This manuscript was published by Superconductor Science & Technology (SuST, IOP) 27, No. 4, 044008, (2014).

Size-controlled spontaneously segregated Ba_2YTaO_6 nanoparticles in $YBa_2Cu_3O_7$ nanocomposites by chemical solution deposition

M.Coll[1], R.Guzman[1], P.Garcés[1,2], J.Gazquez[1], V.Rouco[1], A. Palau[1], S.Ye[1,4], C. Magen[3], H.Suo[4], H.Castro [2], T.Puig[1], X.Obradors[1]

[1]*Institut de Ciència de Materials de Barcelona, ICMAB-CSIC, Campus UAB, 08193, Barcelona, Spain*

[2] *Universidad Nacional de Colombia, Bogotá D.C., Colombia*

[3]*Universidad de Zaragoza, Instituto de Nanociencia de Aragon, Zaragoza 50018, Spain*

[4]*The Key Laboratory of Advanced Functional Materials, Ministry of Education, Beijing University of Technology, Beijing 100124, China*

Corresponding author: mcoll@icmab.es

Abstract

We present a thorough study of the nucleation and growth process of the solution-based $YBa_2Cu_3O_7$-Ba_2YTaO_6 (YBCO-BYTO) system to control the characteristics of the BYTO phase to meet the requirements for specific power applications. Scanning transmission electron microscopy and X-ray diffraction have been used to characterize the BYTO nucleation and phase evolution during the YBCO-BYTO conversion. At high BYTO loads (>10%M), the nanoparticles tend to aggregate being much less efficient for generating nanostrained areas in the YBCO matrix and enhancing the vortex pinning. Our experiments show that by modifying the nucleation kinetics and thermodynamics of the BYTO, the nucleation mode (homogeneous versus heterogeneous), the particle size and their orientation can be controlled. We demonstrate that YBCO-BYTO nanocomposites with high concentration of nanoparticles can be prepared obtaining small and randomly oriented nanoparticles (i.e. high incoherent interface) generating highly strained nanoareas in the YBCO with an enhancement on the vortex pinning. We have also observed that the incoherent interface is not the only parameter that controls the nanostrain. The Cu-O intergrowths characteristics must be a key factor to also control the nanostrain for future tuning the YBCO vortex pinning.

1. Introduction

In recent years, massive work has been devoted to the preparation of epitaxial $YBa_2Cu_3O_7$ (YBCO) superconducting nanocomposite thin films demonstrating that the presence of metal oxide nanoparticles in the YBCO matrix generates nano-scale defects to act as pinning centers for vortices which are responsible for the strong performance improvement [1, 2]. The exceptional properties of YBCO nanocomposite materials depend on the composition, crystal structure, morphology and size of the individual components but they are mostly due to the characteristics of interfaces between the different phases present in the system [2-9]. The interfacial atomic configurations

This manuscript was published by Superconductor Science & Technology (SuST, IOP) 27, No. 4, 044008, (2014).

(chemical nature, structure and orientation) and, consequently, the associated strains and the surface energies [10] provide a fascinating pathway to atomic-level engineering of YBCO microstructure and performance.

The pinning efficiency of the chemical solution derived-YBCO nanocomposites has been recently correlated to the nanostrain generated within the YBCO matrix ensuing from partial dislocations associated to intergrowths (extra Cu-O chain layer). The presence of these structural defects is attributed to the incoherent interface between the nanoparticles and the YBCO matrix, which mainly arises from the percentage of randomly oriented nanodots and the particle size [2, 11, 12]. Therefore, the control of the nanoparticle characteristics within the YBCO matrix and the structural defects in the superconductor are of fundamental importance for the development of high current coated conductors to be used under high magnetic fields [12-14].

Rare-earth niobiates and tantalates (double perovskite $Ba_2RE(Ta,Nb)O_6$ and pyrochlore RE_3TaO_7 with RE=Yb^{3+}, Gd^{3+}, Er^{3+}) have gained attention as effective artificial pinning centers to enhance YBCO properties [11, 15-18]. In particular, the CSD YBCO-Ba_2YTaO_6 (YBCO-BYTO) system offers great potential to further enhance the YBCO nanocomposite performance as it shows the highest percentage ever of random nanoparticles segregated within an epitaxial superconducting matrix [11]. However, at a certain load (≥ 10% M), the nanoparticles tend to agglomerate producing a blocking effect on the YBCO matrix degrading its performance and the nanostrain values saturate [2, 11]. In order to have a better control of the formation process of the nanocomposite and consequently meet the requirements for specific applications, it is crucial to elucidate the origin of this strain/performance saturation.

In this work we describe a thorough study of the nucleation and growth process of the solution-based YBCO-BYTO system to control the nanoparticle size, and their influence on both the generation of the structural defects in the superconducting matrix and the pinning properties. From quench studies we show that the BYTO phase randomly nucleates within the precursor matrix, before the heteroepitaxial growth of the YBCO. The early nucleation and fast growth of BYTO favor nanoparticle aggregation for compositions beyond 10% M with the formation of large extra Cu-O chains in the YBCO matrix. The control of the nucleation kinetics and thermodynamics of BYTO and YBCO phases permit tight control of nanoparticle orientation, size and distribution. The use of a two-step heating profile ensures the formation of highly epitaxial and strained YBCO matrix with >90% randomly oriented nanoparticles where nanoparticle

This manuscript was published by Superconductor Science & Technology (SuST, IOP) 27, No. 4, 044008, (2014).

size has been decreased from 40-60 nm down to 15-20 nm, i.e. enhancing the incoherent interface. Also, we propose that the Cu-O intergrowth characteristics (density, distribution and size) could also control the nanostrain and thus be a relevant parameter to further improve the YBCO pinning properties.

2. Experimental details

Chemical solution deposited 0.25 μm YBCO-BYTO thin films were prepared on 5x5 mm^2 commercially available (100) $LaAlO_3$ (LAO) single crystal substrates from a metalorganic precursor solution containing stoichiometric amounts of tantalum (V) ethoxide (Sigma-Aldrich) in a TFA-YBCO solution. Solution deposition, standard growth and oxygenation conditions have been described elsewhere [11]. Schematics of the heating profiles used in this work to study the phase evolution of YBCO-BYTO system are shown in Scheme 1. Scheme 1(a) corresponds to the standard high temperature thermal treatment (conversion and oxygenation) previously described for YBCO-BYTO films [11]. Scheme 1(b) corresponds to the general profile of quench experiments performed from different temperatures (500ºC-815ºC) and annealing times (0 min to 180 min). Finally, the scheme of a two-step conversion profile and oxygenation process is shown in scheme 1(c). The microstructure and phase analysis of the partially and fully converted YBCO nanocomposite films were studied by 2D X-ray diffraction (XRD) using a Bruker AXS GADDS diffractometer. Strain quantification (ε) was carried out based on the Williamson-Hall method [19, 20], by analyzing the symmetric (00l) 2θ Bragg diffraction integral breath acquired in a SIEMENS D5000 diffractometer. Quantitative determination of the randomly oriented nanodot fraction (RF) was performed by 2D-XRD analysis based on a simultaneous out-of-plane measurement of both textured and random signals [2]. Scanning Transmission Electron Microscopy (STEM) and electron energy loss spectroscopy (EELS) studies using a Fei-TITAN 60-300 microscope equipped with a X-FEG gun, a CETCOR probe corrector and a Gatan energy filter TRIDIEM 866 ERS operated in STEM at 300 kV was carried out to evaluate nanoparticle size, distribution and atomic scale defects. Critical current densities (J_c) and critical temperatures (T_c) were obtained by SQUID magnetron measurements. Transport measurements were performed in a 9T cryostat on 200 μm x 20 μm tracks using a 1 μV cm^{-1} criterion. Pinning landscape analysis was evaluated by

This manuscript was published by Superconductor Science & Technology (SuST, IOP) 27, No. 4, 044008, (2014).

measuring J_c (H) and applying the Blatter scaling approach to separate and quantify the isotropic and anisotropic pinning contributions.

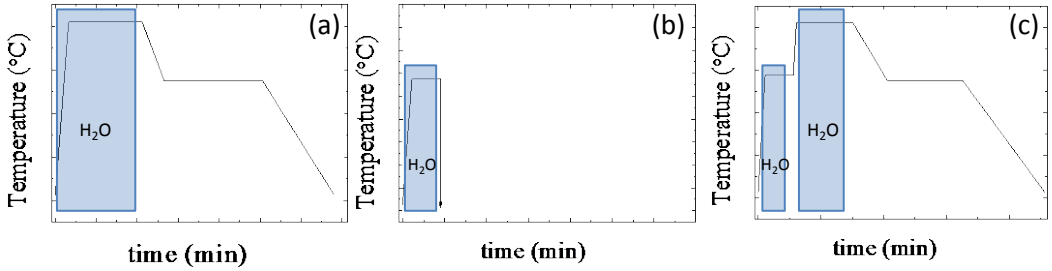

Scheme 1. Schematic of the heating profiles studied to prepare YBCO nanocomposites and generate small and homogeneously distributed second phases. (a) standard conditions [11], (b) quench performed at intermediate temperatures (500-815ºC) (c) two step heating profile.

3. Results and discussions

Typical two dimensional θ-2θ X-ray diffraction (XRD) pattern of YBCO-10%BYTO nanocomposite thin films prepared following the standard heating profile (scheme 1(a)) is shown in the inset of figure 1(a). The (00l) diffraction spots of the YBCO phase reveal ***c***-axis orientation ((001) plane parallel to the LAO substrate) and the BYTO rings from the (220) and (400) reflections indicate this minority phase is mostly randomly oriented (RF=95%). High resolution Z-contrast image of YBCO-10%BYTO nanocomposites show that beside isolated BYTO nanoparticles, the second phase can also aggregate resulting in nanoparticles with diameter sizes ranging from 40 to 80 nm, see Figure 1(a). From a higher magnification Z-contrast image, Figure 1(b), it can be clearly identified the coalescence of three nanoparticles along with high density of extra Cu-O chains (horizontal dark stripes in the image) with typical lateral extension of ~100 nm in diameter. These defects consisting of an extra Cu-O chain in the YBCO structure are identified as the well known $Y_2Ba_4Cu_8O_{16}$ phase (Y248) [21, 22]. These processing conditions lead to T_c =90K and J_c @77K= 1.5 MA/cm^2. The aggregated randomly oriented nanoparticles expose less interfacial area to the epitaxial superconducting matrix, i.e. less incoherent interface, than the three separate nanoparticles. In this scenario, the nanoparticles are much less efficient in terms of generating nanostrained areas in the YBCO matrix, which could explain the saturation of the ε, and at higher nanoparticle loads it could also contribute to the drop in pinning efficiency below the pristine film, as previously reported [2, 11]. In order to prepare

This manuscript was published by Superconductor Science & Technology (SuST, IOP) 27, No. 4, 044008, (2014).

CSD-YBCO nanocomposites, even at high nanoparticle concentrations, it is mandatory to first control the nanoparticle size, orientation and distribution. However, investigations of the synthesis variables in solution derived complex oxide nanocomposites are scarce [14, 23-25].

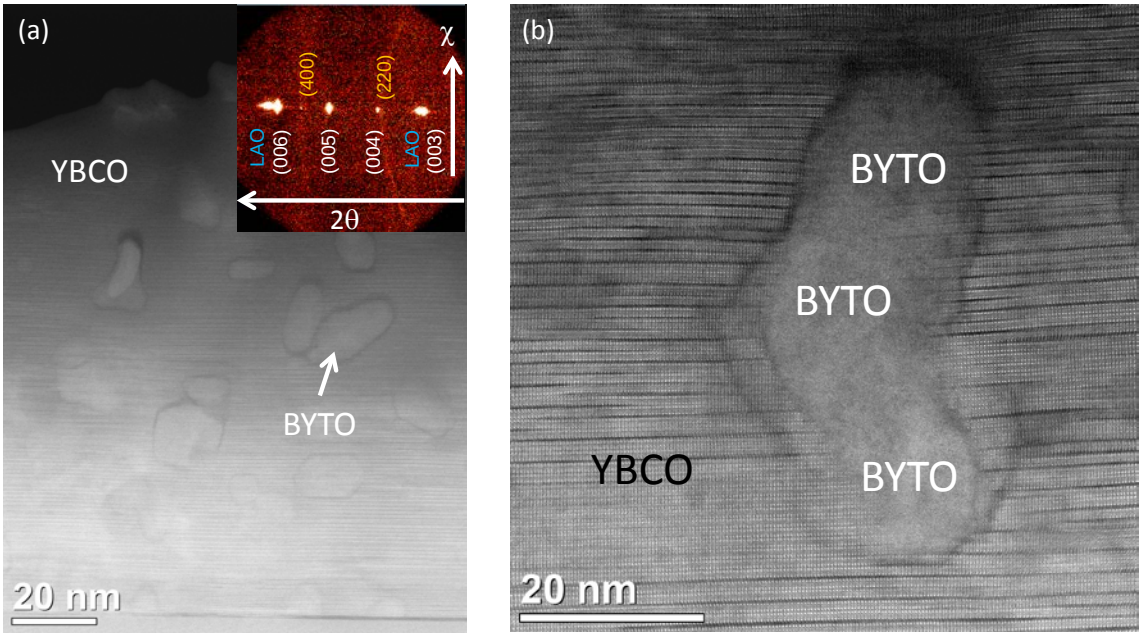

Figure 1. (a) Low magnification Z-contrast image of YBCO-10%BYTO nanocomposite film with the corresponding 2D-XRD θ-2θ diffraction pattern (b) High magnification Z-contrast image of an aggregated BYTO nanoparticle embedded in the YBCO matrix with a high density of Cu-O defects (horizontal dark stripes). This film has been prepared following the standard high temperature thermal process (scheme 1(a)).

In order to avoid the coalescence of the spontaneously segregated BYTO nanoparticles, BYTO nucleation temperature should be considered. Integrated XRD θ-2θ patterns of quenched samples from several intermediate temperatures (600-815ºC) are shown in Figure 2. At 600ºC, the nanocomposite film consists of $Ba_{1-x}Y_xF_{2+x}$ (BYF) and CuO phases. By increasing the quenched temperature up to 750ºC, the BYF peaks shift to lower 2θ values according to the formation of Ba oxyfluoride (OF) and the release of Y from the structure [26]. At 775ºC, $Y_2Cu_2O_5$ and Ba_2YTaO_6 phases are first identified. The shallow rings observed in the 2D X-ray diffraction pattern from this sample, figure 2(b), reveal that the intermediate phases show poor crystallinity. At higher temperature (815ºC), CuO, OF and $Y_2Cu_2O_5$ phases are consumed to form (00l)

This manuscript was published by Superconductor Science & Technology (SuST, IOP) 27, No. 4, 044008, (2014).

oriented YBCO peaks indicating the nucleation of *c*-axis oriented YBCO films. Regarding the BYTO second phase evolution, Z-contrast image and EELS elemental analysis demonstrate that at 815 ºC and 0 min, large BYTO nanoparticles exist within the precursor YBCO matrix, see figure 3. The fact that the BYTO nanoparticles nucleate embedded inside the random nanocrystalline oxy-fluoride intermediate phase, could explain the random orientation of the BYTO nanodots. Therefore, it is expected that the epitaxial YBCO growth front surrounds the existing randomly oriented nanodots generating the incoherent interface until the heteroepitaxial YBCO growth completion, as previously identified in solution-derived YBCO films with simple perovskite second phases [13, 27]. The large size of the BYTO nanoparticles within the precursor matrix suggests that BYTO growth is rather fast.

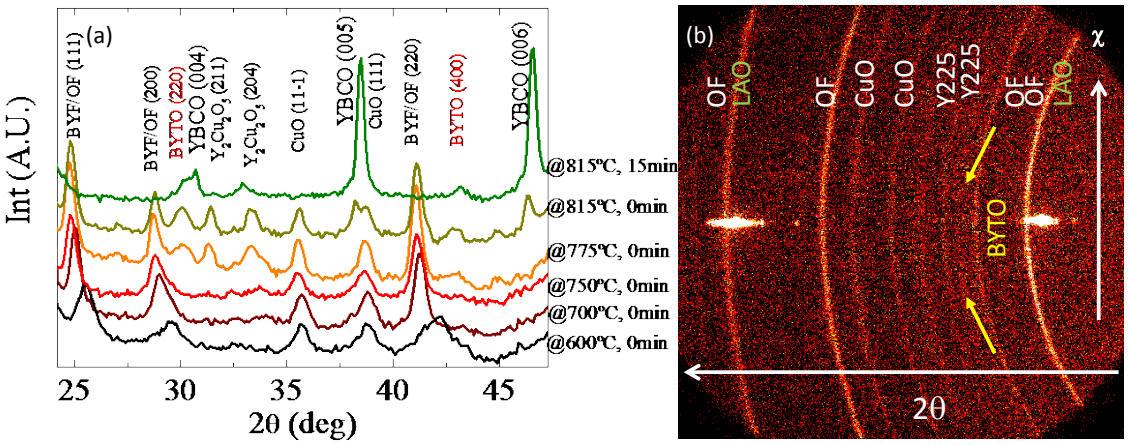

Figure 2. 2D X-ray diffraction study of YBCO-10% BYTO/LAO films quenched from different temperatures. (a) Integrated θ-2θ scans (b) 2D- XRD pattern of the film quenched from 775ºC. Arrows indicate the ring corresponding to the (220) BYTO reflection.

To shed light on the BYTO nanoparticle aggregation, nucleation and growth kinetics have been investigated. Based on the XRD data shown above, it is likely that the complex phase evolution of YBCO in the YBCO-BYTO nanocomposite film proceeds similarly to the pristine YBCO films following the primary chemical reaction [26, 28, 29]

$$Ba(O_xF_y)_2 + \frac{3}{2}CuO + \frac{1}{4}Y_2O_3 + yH_2O \rightarrow \frac{1}{2}YBa_2Cu_3O_{6.5} + 2y\,HF \qquad \text{eq.1}$$

From this reaction it is well established that P(H_2O) is a relevant, but not exclusive, parameter to control the conversion of the YBCO thin films [29-34]. Although no Ta-

This manuscript was published by Superconductor Science & Technology (SuST, IOP) 27, No. 4, 044008, (2014).

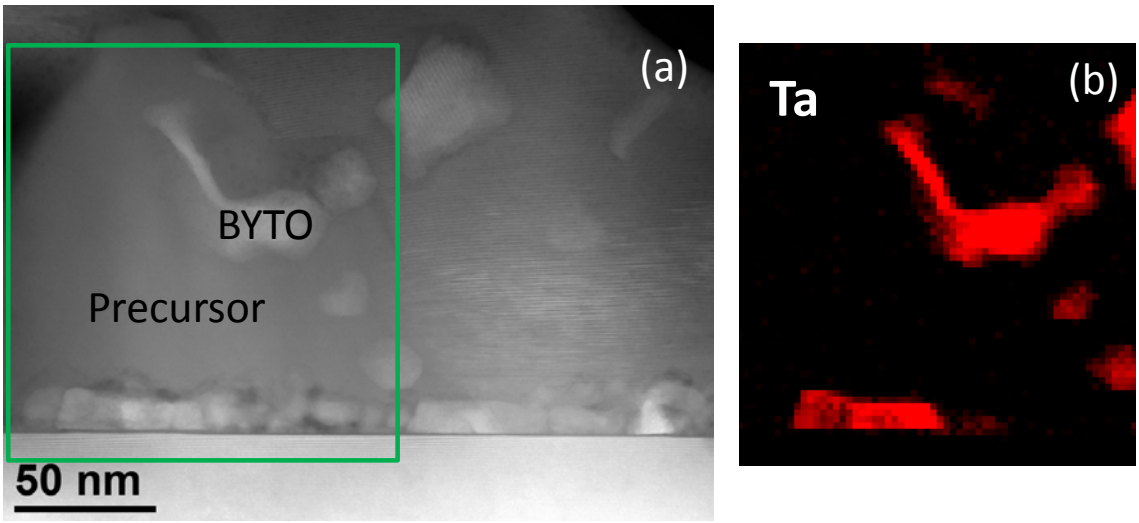

Figure 3. (a) Low magnification Z-contrast image from a YBCO -10%BYTO /LAO thin film quenched from 815ºC, 0 min. The square marks the region from which the spectrum image was acquired. (b) EELS elemental map of Ta M-edge acquired from (a). Map is in false color.

based intermediate phases have been detected to help predicting the Ba_2YTaO_6 conversion, it is assumed that changes in the $P(H_2O)$ will also influence the evolution of this double perovskite phase, since Ba and Y sources ($Ba(O_xF_y)_2$ and Y_2O_3) are also required to from BYTO. In addition, the nucleation of a material without the addition of foreign materials (homogeneous) requires a large driving force because of the relatively large contribution of the surface energy of very small nanoparticles. The thermodynamic barrier to nucleate a new phase decreases with increasing undercooling (ΔT), ΔG_i^*. Assuming spherical crystallites,

$$\Delta G_i^* \propto \frac{1}{\Delta T^2} \qquad \text{eq.2}$$

When the nucleation takes place on the substrate (heterogeneous), the large thermodynamic barrier to homogeneous nucleation can be modified by a factor *f(θ)*,

$$\Delta G_{heter}^* = \Delta G_i^* f(\theta) \qquad \text{eq.3}$$

where θ would be the contact angle between the nuclei and the substrate surface [35]. In general, when the wetting between the crystal and substrate improves, the nucleation barrier also decreases. From the nucleation rate dependence with undercooling [35], it is expected that the homogeneous nucleation will be promoted at low temperature. The competition between the heterogeneous and homogeneous nucleation is especially important in cases where a particular orientation of the crystal is required, as in the case of YBCO coated conductors. For CSD-YBCO, it has been described a Volmer-Weber heterogeneous nucleation mechanism where ***c***-axis oriented YBCO islands are formed

This manuscript was published by Superconductor Science & Technology (SuST, IOP) 27, No. 4, 044008, (2014).

at the interface with the substrate under low supersaturation conditions. Importantly, the supersaturation can be modified and preferred *c*-axis orientation can also be achieved by properly tuning of $P(H_2O)$ or total pressure P(T) [33, 36].

Based on that, we have investigated the microstructural scenario when the nucleation of YBCO and BYTO phases is imposed to simultaneously occur at the annealing temperature (i.e. adding H_2O to the system only at the annealing temperature). Z-contrast imaging reveals the formation of very large epitaxial BYTO nanoparticles (i.e. 100 nm) on the substrate surface, maintaining epitaxial YBCO matrix, see figure 4(a). Figure 4(b) shows a Z-contrast high resolution image of an YBCO/BYTO interface. As observed, the shared epitaxial relationship corresponds to a cube-on-cube epitaxy, i.e. $(001)[010]_{YBCO}||(001)[010]_{BYTO,}$ with a slight misalignment of the BYTO structure of about 4º. From the 2D-XRD θ-2θ frame, inset figure 4(a), it is observed that (400) Bragg reflection from BYTO predominates, which is in agreement with experimental STEM images. Note that the ring previously identified from (220) BYTO at 2θ=29.9º in figure 1(a) has vanished. Also (00l) YBCO are identified with a small fraction of (103) YBCO. From simultaneous out-of-plane 2D XRD analysis [11] it has been obtained that the BYTO random fraction has decreased from ~ 90% down to 34%, in well agreement with the absence of the intense ring from the (220) BYTO Bragg reflection in the inset of Figure 4. Thus, by delaying the nucleation of BYTO at 815ºC, the heterogeneous nucleation of BYTO is favorable over the homogeneous nucleation forming epitaxial BYTO nanoparticles on the substrate surface. It is expected that at high temperature the wetting between the nuclei and the substrate ($f(\theta)$) improves and the heterogeneous nucleation barrier decreases, consistent with the nucleation theory [35]. For these processing conditions, the critical current density (J_c) at 77K is 0.5MA/cm^2, considerably lower compared to the values obtained for this composition following the standard processing conditions (3-4 MA/cm^2). This decrease in J_c could be explained by the presence of disordered YBCO grains previously identified from XRD and the blocking effect of the large BYTO nanoparticles in the current percolation [11].

This manuscript was published by Superconductor Science & Technology (SuST, IOP) 27, No. 4, 044008, (2014).

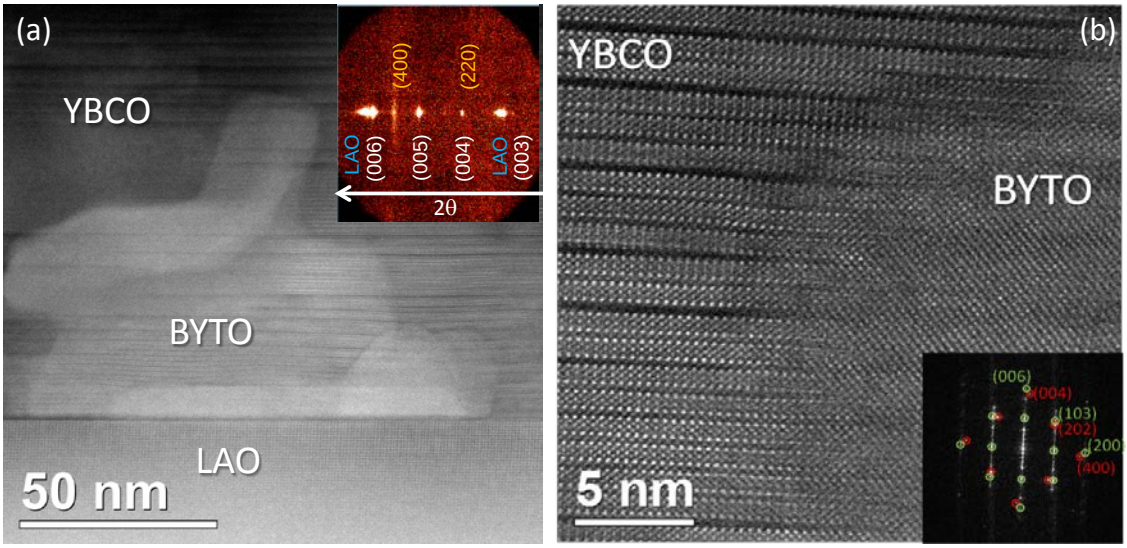

Figure 4 (a) Z-contrast image of a large epitaxially oriented BYTO nanoparticle onto the substrate surface. (b) Z-contrast high resolution image of the same nanoparticle showing a $(001)[010]_{YBCO}||(001)[010]_{BYTO}$ epitaxial relationship. The inset is the corresponding FFT (green and red labels correspond to YBCO and BYTO, respectively). Dark horizontal stripes are Y248 intergrowths.

With the aim to control and hinder BYTO coalescence in an homogeneous nucleation regime, it has been investigated the BYTO phase evolution when the film is exposed to different annealing times at a temperature below the nucleation temperature identified in Figure 2, i.e. 775ºC. A pyrolysed film and a series of quenched YBCO-BYTO films from 575ºC annealed for 10, 25, 85 and 180 min have been investigated by X-ray diffraction, see Figure 5. The pyrolysed film consists of BYF and CuO phases, in agreement with previous YBCO phase evolution studies [26, 28]. By increasing the annealing time at 575ºC from 10 min to 85 min, CuO peaks decrease in intensity while BYF phase evolutes to OF. At 575ºC for 85 min it is identified the (220) BYTO reflection indicating the presence of the BYTO nuclei. Longer annealing time, 180 min, (220) BYTO peaks increase in intensity and BYTO (400) is clearly identified. We also note that the sample quenched from 575ºC after 180 min shows the (00l) and (103) YBCO reflections, suggesting epitaxial and partial random orientation of YBCO [28].

Annular Dark-Field (ADF) Z-contrast images performed on the sample quenched at 575ºC for 85 minutes shows the formation of a porous film consistent with the low processing temperature, figure 6. In order to study the elemental composition of the quenched film, the sample has been analyzed by EELS. EEL spectrum imaging revealed the presence of Ba, Cu, O, Y, Ta and F in well agreement with the intermediate phases detected by XRD in figure 5. It is important to note that the size of the particles

This manuscript was published by Superconductor Science & Technology (SuST, IOP) 27, No. 4, 044008, (2014).

containing Ta is very small, ~5-10 nm, compared to the final size identified in the standard process, see figure 1(a). Closer look at the EEL spectrum images show two different compositions for Ta phase: BYTO and Ba-Ta-O. This data confirms that performing a short dwell at 575ºC, allows the homogeneous nucleation of small BYTO nanoparticles.

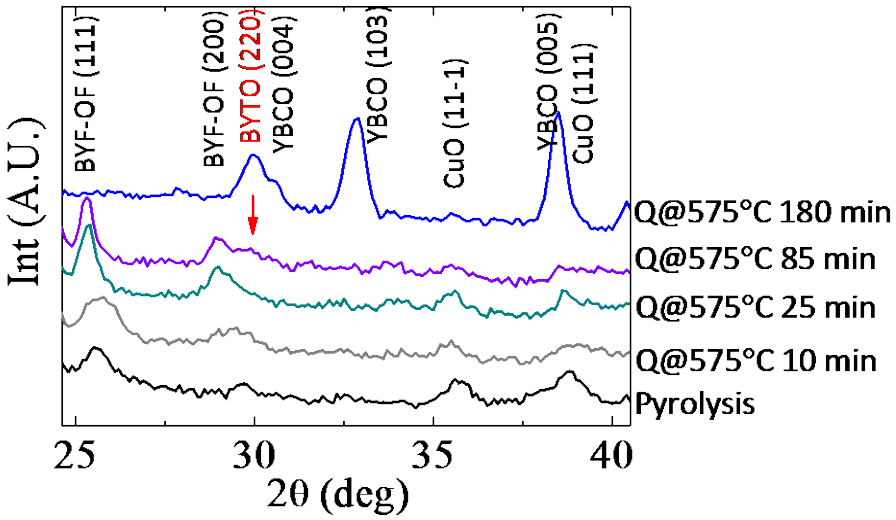

Figure 5. X-ray diffraction integrated θ-2θ scan of YBCO-10%BYTO samples at different stages of the growth process : pyrolysis, quenched at 575ºC 10 min, 25 min, 85 min and 180 min.

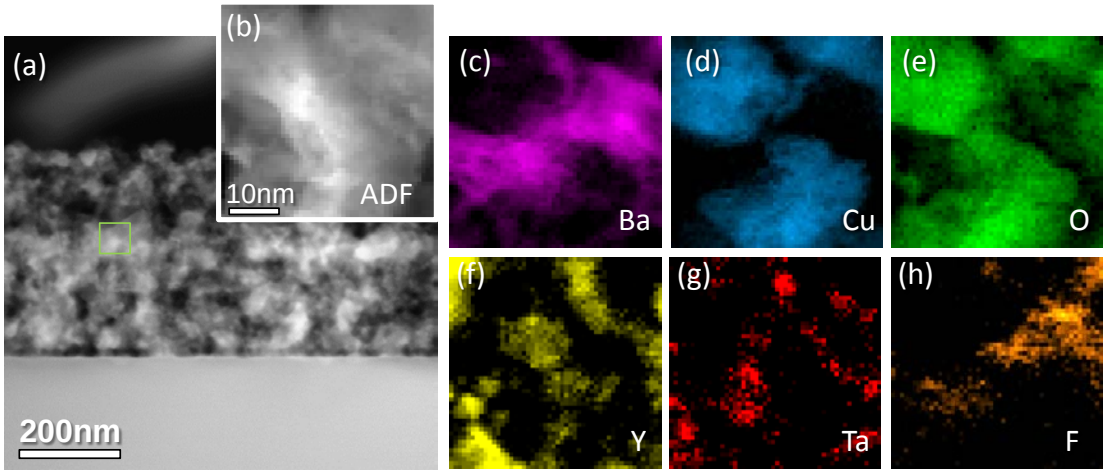

Figure 6. Z-contrast image of YBCO-10%BYTO quenched at 575ºC 85 min. The square marks the region from which the spectrum image was acquired. (b) simultaneous annular dark field (ADF) signal image (c)-(h) EEL spectrum image of Ba M-edge (purple), Cu L-edge (blue), O K-edge (green), Y L-edge (yellow), Ta M-edge (red) and F K-edge (orange), respectively. Maps are in false color.

This manuscript was published by Superconductor Science & Technology (SuST, IOP) 27, No. 4, 044008, (2014).

A two step heating profile was designed in order to separate BYTO and YBCO nucleation and growth process, scheme 1(c). It is important to note that the second heating ramp (from 575ºC to 815ºC) has been performed under dry atmosphere to minimize the coalescence of the already nucleated BYTO nanoparticles. 2D X-ray diffraction θ-2θ scan shows the presence of (00l) YBCO peaks indicating the formation of ***c***-axis oriented superconducting film, see figure 7. Also, BYTO peaks are clearly identified with a random fraction of 93%.

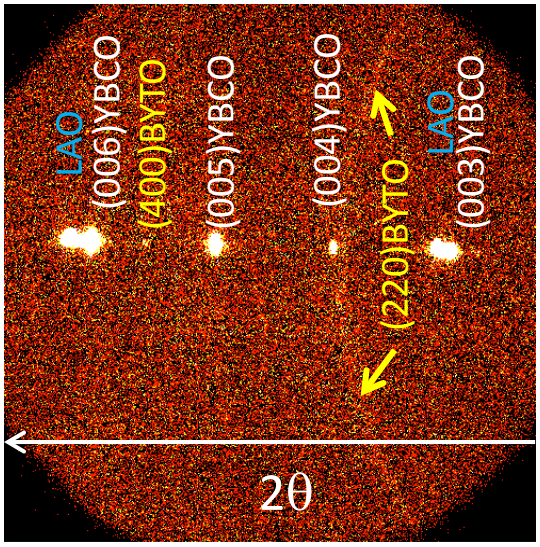

Figure 7. 2D-XRD θ-2θ scan of YBCO+10%BYTO thin film prepared using the two step heating profile.

These conditions favor the homogeneous nucleation of BYTO, with a significant drop in particle size, down to ~15-20 nm as will be discussed below, and consequently, the generation of 0.27% of nanostrain. This nanostrain value is significantly enhanced compared to the sample grown from the traditional single step heating profile (0.22%). These processing conditions do not degrade the YBCO critical temperature, T_c = 90K, and lead to critical current densities at 77K of 2.3 MA/cm^2. Figure 8 shows the nanostrain as a function of the incoherent interface obtained for a series of YBCO-BYTO system grown under the standard process with different amount of BYTO nanoparticles. Data from a YBCO-10%BYTO system processsed under the two step heating profile (blue symbol) and a standard composite with 10%M of $BaZrO_3$ (YBCO-10%BZO) (red symbol) are also included [2]. A clear relation between the incoherent interface and the nanostrain generated within the YBCO matrix for YBCO-BYTO

This manuscript was published by Superconductor Science & Technology (SuST, IOP) 27, No. 4, 044008, (2014).

system is observed. The use of a two step heating profile is obviously efficient to increase the incoherent interface and thus the nanostrain. However, when comparing with the general trend previously reported [2], the YBCO-BZO system seems to present a higher slope. This suggests the enhancement of the incoherent interface is not the only parameter to control the nanostrain, and will be further discussed in figure 10.

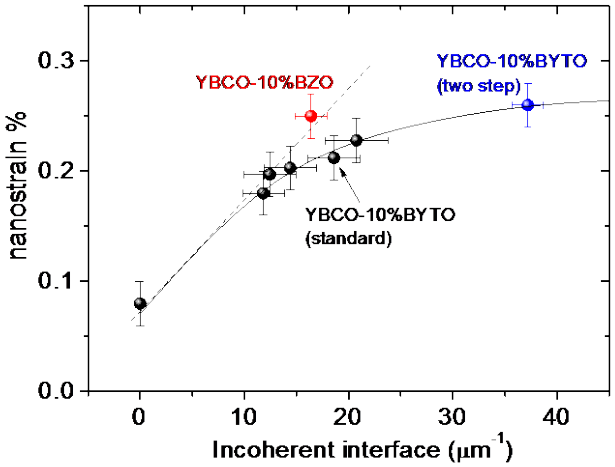

Figure 8. Dependence of the YBCO nanostrain on the incoherent interface of nanodots in YBCO- BYTO films processed under the standard process. Arrow shows the YBCO-10%BYTO film on this series. Data from the YBCO-10%BYTO system processed using the two step heating profile and from a standard nanocomposite with BZO nanoparticles (YBCO-10%BZO)[2]. Lines are guide for the eyes.

At this point, it is important to evaluate how these changes in the nanostrain and incoherent interface influence the pinning properties of the YBCO nanocomposite. Figure 9(a) shows the mangetic field dependence of the normalized critical current density for a pristine YBCO film and the YBCO-10%BYTO system processed under a single and a two step process. A much smoother $J_c(H)$ dependence is observed in YBCO-BYTO systems compared to the pristine film as previously reported [11], and the two step YBCO-10%BYTO film shows an enhancement of $J_c(H)$ compared to the standard YBCO-10%BYTO. When it is evaluated the dependence of the maximum isotropic pinning force (F^{iso}_{max}) with the nanostrain, figure 9(b), it is observed that the two step heating profile sample follows the existing trend [2].

This manuscript was published by Superconductor Science & Technology (SuST, IOP) 27, No. 4, 044008, (2014).

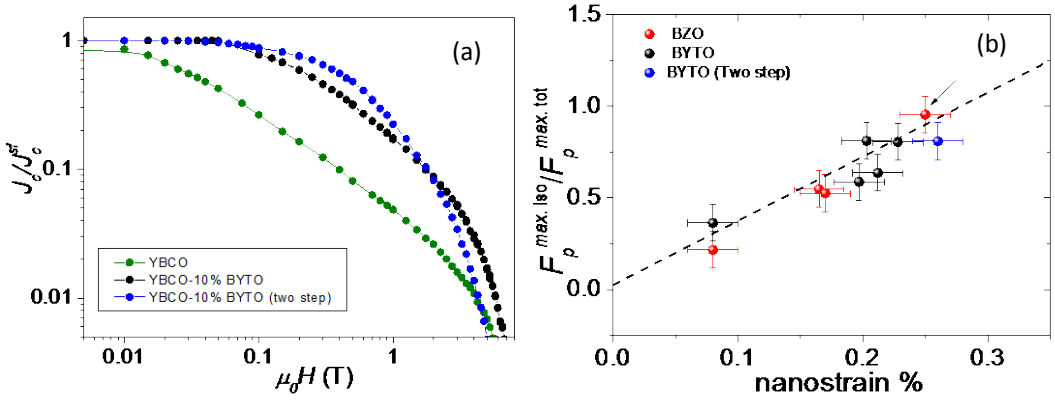

Figure 9.(a) Normalized critical current density versus magnetic field at 77 K in YBCO-10%BYTO nanocomposites processed under the standard and the two step heating process. (b)Dependence of the normalized maximum isotropic pinning force $F^{iso}_{pmax}/ F^{tot}_{pmax}$ on the nanostrain of the YBCO-BYTO nanocomposites prepared following the standard process (black), using the two step process (blue) and compared to the YBCO-BZO system (red). Arrow indicates the YBCO-10%BZO nanocomposite.

Extra microstructural analysis has been carried out in order to evaluate the YBCO structural defects that can be generated by the BYTO and could influence the nanostrain, see figure 10. Figure 10(a) corresponds to YBCO-10% BYTO sample processed following the standard heating profile resulting coalescence (nanoparticle size up to 80 nm) and high density of Y248 intergrowths (50-100 nm of lateral extension) [2] generating a 0.22% of nanostrain. Figure 10(b) corresponds to the YBCO-10%BYTO sample processed following the two-step heating profile. This image shows the formation of small nanoparticles (15-20nm) and similar scenario of Y248 intergrowths. The obtained nanostrain is 0.27%. As we mentioned above, this route allows us to increase the incoherent interface although the nanostrain is not as high as could be expected if BYTO would follow the general linear trend. Next, we compare samples with the same nanoparticle size and different nanostrain. Figure 10(c) and figure 10(d) corresponds to YBCO-6%BYTO samples processed under different conditions with a nanostrain of 0.21% and 0.23%, respectively. Both samples show the same nanoparticle size (20-25 nm) and the main difference is the Y248 intergrowth landscape. Whereas figure 10(c) shows Y248 intergrowths with high lateral extension, figure 10(d) shows much shorter Y248 intergrowths. From this microstructural analysis we suggest that the characteristics of the Y248 intergrowths, their density, distribution and size must contribute to the nanostrain and be a relevant parameter to tune and further increase the vortex pinning. Effort in indentifying the correlation between these factors and the vortex pinning properties need to be done in the future.

This manuscript was published by Superconductor Science & Technology (SuST, IOP) 27, No. 4, 044008, (2014).

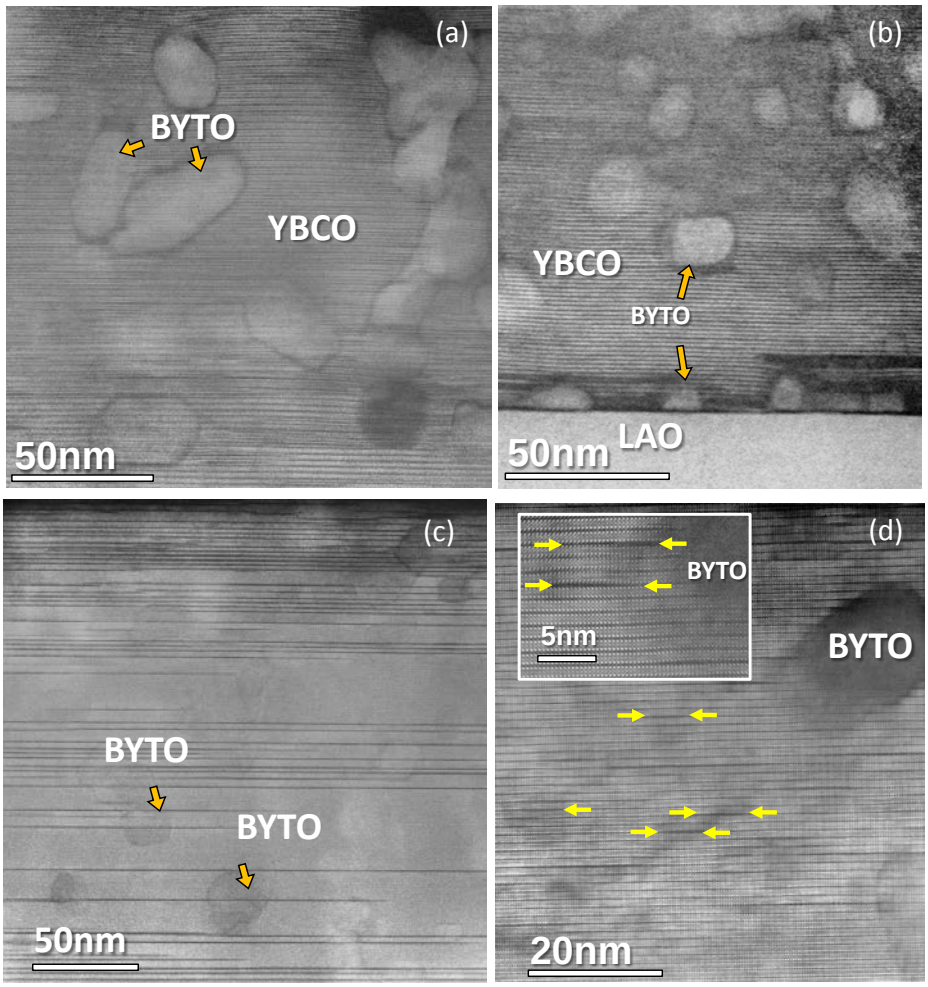

Figure 10. Z-contrast images of (a) YBCO-10%BYTO thin film with ε~0.22%, (b) YBCO-10%BYTO thin film with ε~0.27% . (c) YBCO-6%BYTO thin film with ε~0.21% and (d) YBCO-6%BYTO thin film with ε~0.23% . The inset in (d) shows a higher magnification of this image. Yellow arrows indicate some of the stacking faults.

4. Conclusions

The versatility of CSD route offers a unique opportunity to generate specific film nanostructures by properly tuning the evolution from the nanostructured to epitaxial forms by playing with the processing conditions. The fast nucleation and growth of BYTO within the YBCO precursor matrix favor nanodot aggregation for compositions beyond 10% M. Controlling the kinetics and the thermodynamic barrier for BYTO nucleation is a very effective and simple route to prepare small, randomly oriented and homogeneously distributed nanoparticles (i.e., high incoherent interface), even at high nanoparticle loads, while enabling epitaxial growth and nanostrained YBCO matrix.

This manuscript was published by Superconductor Science & Technology (SuST, IOP) 27, No. 4, 044008, (2014).

Also, using this modified process we have further supported the existing correlation between the maximum isotropic pinning force and the nanostrain. Finally, we suggest that the incoherent interface is not the only parameter that allows controlling the nanostrain but also the characteristics of the Y248 intergrowth. This could enable further enhancement of the vortex pinning in YBCO.

Acknowledgements

The authors would like to thank the financial support of MICINN (MAT2008-01022), Consolider NANOSELECT (CSD2007-00041), and Generalitat de Catalunya (2009 SGR 770, NanoAraCat and Xarmae) and EU (EUROTAPES, FP7/2007-2013) and NanoSC COST action MP1201. R.G and M.C thank the grants of MICINN, J.G thanks JAE CSIC grants. S.Y would like to thank the National Natural Science Foundation of China (51171002) and the program of New Century Excellent Talents in University of China. Authors acknowledge LMA-INA for offering access to their instruments and expertise.

References

[1] Gutierrez J, Llordes A, Gazquez J, Gibert M, Roma N, Ricart S, Pomar A, Sandiumenge F, Mestres N, Puig T and Obradors X 2007 *Nat. Mater.* **6** 367
[2] Llordes A, Palau A, Gazquez J, Coll M, Vlad R, Pomar A, Arbiol J, Guzmán R, Ye S, Rouco V, Sandiumenge F, Ricart S, Puig T, Varela M, Chateigner D, Vanacken J, Gutierrez J, Moshchalkov V, Deutcher G, Magen C and Obradors X 2012 *Nat. Mater.* **11** 329
[3] Abellan P, Sandiumenge F, Casanove M J, Gibert M, Palau A, Puig T and Obradors X 2011 *Acta Materialia* **59** 2075
[4] Aytug T, Paranthaman M, Leonard K J, Kang S, Martin P M, Heatherly L, Goyal A, Ijaduola A O, Thompson J R, Christen D K, Meng R, Rusakova I and Chu C W 2006 *Physical Review B* **74**
[5] Cantoni C, Gao Y F, Wee S H, Specht E D, Gazquez J, Meng J Y, Pennycook S J and Goyal A 2011 *Acs Nano* **5** 4783
[6] Kang S, Goyal A, Li J, Gapud A A, Martin P M, Heatherly L, Thompson J R, Christen D K, List F A, Paranthaman M and Lee D F 2006 *Science* **311** 1911
[7] Mastorakos I N, Bellou A, Bahr D F and Zbib H M 2011 *J. Mater. Res.* **26** 1179
[8] Mastorakos I N, Zbib H M and Bahr D F 2009 *Appl. Phys. Lett.* **94** 3
[9] MacManus-Driscoll J L 2010 *Adv. Funct. Mater.* **20** 2035
[10] Shi J J and Wu J Z 2012 *Philos Mag* **92** 2911
[11] Coll M, Ye S, Rouco V, Palau A, Guzman R, Gazquez J, Arbiol J, Suo H, Puig T and Obradors X 2013 *Supercond. Sci. Technol.* **26**
[12] Guzman R, Gazquez J, Rouco V, Palau A, Magen C, Varela M, Arbiol J, Obradors X and Puig T 2013 *Appl. Phys. Lett.* **102**
[13] Miura M, Yoshizumi M, Izumi T and Shiohara Y 2010 *Supercond. Sci. Technol.* **23**

This manuscript was published by Superconductor Science & Technology (SuST, IOP) 27, No. 4, 044008, (2014).

[14] Miura M, Maiorov B, Willis J O, Kato T, Sato M, Izumi T, Shiohara Y and Civale L 2013 *Superconductor Science and Technology* **26** 035008
[15] Babu T G N and Koshy J 1997 *Materials Letters* **33** 7
[16] Feldmann D M, Holesinger T G, Maiorov B, Foltyn S R, Coulter J Y and Apodaca I 2010 *Supercond. Sci. Technol.* **23** 095004
[17] Harrington S A, Durrell J H, Maiorov B, Wang H, Wimbush S C, Kursumovic A, Lee J H and MacManus-Driscoll J L 2009 *Supercond. Sci. Technol.* **22** 022001
[18] Wee S H, Goyal A, Specht E D, Cantoni C, Zuev Y L, Selvamanickam V and Cook S 2010 *Phys. Rev. B* **81** 140503
[19] Popa N C 1998 *Journal of Applied Crystallography* **31** 176
[20] Williamson G K and Hall W H 1953 *Acta Metallurgica* **1** 22
[21] Gazquez J and al. e in preparation
[22] Gazquez J, Coll M, Roma N, Sandiumenge F, Puig T and Obradors X 2012 *Supercond. Sci. Technol.* **25** 065009
[23] Liu B, Sun T, He J Q and Dravid V P 2010 *Acs Nano* **4** 6836
[24] Roy R 1969 *Journal of the American Ceramic Society* **52** 344
[25] ROY R 1987 *Science* **238** 1664
[26] Gazquez J, Sandiumenge F, Coll M, Pomar A, Mestres N, Puig T, Obradors X, Kihn Y, Casanove M J and Ballesteros C 2006 *Chemistry of Materials* **18** 6211
[27] Puig T, Gutierrez J, Pomar A, Llordes A, Gazquez J, Ricart S, Sandiumenge F and Obradors X 2008 *Supercond. Sci. Technol.* **21** 034008
[28] Zalamova K, Pomar A, Palau A, Puig T and Obradors X 2010 *Supercond. Sci. Technol.* **23**
[29] Obradors X, Martínez-Julián F, Zalamova K, Vlad V R, Pomar A, Palau A, Llordés A, Chen H, Coll M, Ricart S, Mestres N, Granados X, Puig T and Rikel M 2012 *Physica C* **482** 58
[30] Puig T, Gonzalez J C, Pomar A, Mestres N, Castano O, Coll M, Gazquez J, Sandiumenge F, Pinol S and Obradors X 2005 *Supercond. Sci. Technol.* **18** 1141
[31] Solovyov V, Dimitrov I K and Li Q 2013 *Supercond. Sci. Technol.* **26**
[32] Teranishi R, Honjo T, Nakamura Y, Fuji H, Tokunaga Y, Matsuda J, Izumi T and Shiohara Y 2003 *Physica C-Superconductivity and Its Applications* **392** 882
[33] Chen H, Zalamova K, Pomar A, Granados X, Puig T and Obradors X 2010 *J. Mater. Res.* **25** 2371
[34] Chen H, Zalamova K, Pomar A, Granados X, Puig T and Obradors X 2010 *Supercond. Sci. Technol.* **23**
[35] Flemings M C 1974 *Solidification Processing* (Mcgraw-Hill College)
[36] Obradors X, Puig T, Ricart S, Coll M, Gazquez J, Palau A and Granados X 2012 *Superconductor Science and Technology* **25** 123001